

Dynamic scattering of electron vortex beams- a Bloch wave analysis

B.G. Mendis

Dept of Physics, Durham University, Durham, DH1 3LE, UK

Abstract

Two important applications of electron vortex beams are in electron magnetic chiral dichroism (EMCD) measurements and nanoparticle manipulation. In both cases orbital angular momentum ($\langle L_z \rangle$) transfer between the vortex beam and the specimen due to dynamic scattering is critical. In general the $\langle L_z \rangle$ pendellösung consists of short and long wavelength oscillations. The former is due to interference between the tightly bound 1s and more dispersive non-1s Bloch states, while the latter is due to interference between the non-1s states. For EMCD experiments with $\pm\hbar$ angular momentum beams, momentum transfer can be minimised by selecting the appropriate aperture size, so that the probe wavefunction approximately matches that of the 2p-type Bloch states. For manipulating nanoparticles with large angular momentum beams small apertures are required to excite the 1s state and thereby enhance the short wavelength oscillations in $\langle L_z \rangle$. This enables efficient momentum transfer to the specimen, provided the nanoparticle dimension corresponds to a minimum in the $\langle L_z \rangle$ pendellösung.

Keywords: electron vortex beams, angular momentum, electron magnetic chiral dichroism (EMCD), nanoparticle manipulation.

1. Introduction

Vortex beams produced in the electron microscope [1-5] have generated considerable interest due to their potential applications in manipulating nano-objects [6-7] and probing magnetic phenomena [8], including magnetic chiral dichroism [2,9-11]. The vortex beam is characterised by a phase singularity along the beam propagation direction and an orbital angular momentum of $m\hbar$, where m is the winding number of the phase. Electron energy loss spectroscopy (EELS) with $m = \pm 1$ vortex beams is used for electron magnetic chiral dichroism (EMCD) measurements, similar to the X-ray analogue (i.e. XMCD), but with far better spatial resolution. However, these EMCD experiments are intrinsically complicated by several artefacts. First it has been shown both theoretically [10-11] and experimentally [12] that in order to generate a dichroic EELS signal the electron probe must be localised at the ionised atom. This means producing an atomic-scale electron vortex beam, for example by using spiral or pitch fork hologram apertures with large convergence angle [4-5]. Secondly the atomic scale vortex beam must also channel along the atom column of interest, preserving its orbital angular momentum during propagation. Multislice simulations [11,13] however have shown that this is not necessarily the case, due to momentum exchange with the crystal. In contrast, for nanoparticle manipulation, momentum must be transferred from the beam to the specimen as efficiently as possible.

This paper deals with dynamic scattering of electron vortex beams, in the context of EMCD measurements ($m = \pm 1$ beams) and nanoparticle manipulation. The latter is restricted to vortex beams with large angular momentum (e.g. $m=5$). This is because experiments [6] have shown that the nanoparticle rotation induced by $m = \pm 1$ beams is severely damped by frictional forces from the support substrate, and one way to overcome this is to use vortices with large angular momentum (note that vortex beams with angular momentum as large as $100\hbar$ have been created in the electron microscope [3]). Dynamic scattering of the electron vortex beam is analysed using Bloch waves. These are individual solutions to the Schrödinger equation and by linearly combining them the electron wavefunction at any given depth within the crystal can be simulated. Dynamic scattering arises as a result of interference between the excited Bloch states. The Bloch wave method is computationally more suitable for perfect crystals, although perturbation-type theories are available for deformed [14] and chemically doped [15-16] crystals. Nevertheless it has the unique advantage of being physically intuitive. Indeed scattering of a conventional (i.e. $m=0$) focussed probe has frequently been interpreted in terms of the 1s Bloch state [17-19], which has zero angular momentum and is similar to the 1s orbital of an isolated atom column. On this basis it has been proposed [20] that the 2p Bloch states (angular momentum of $\pm\hbar$ for the equivalent atom column orbital) could play a similarly important role for $m = \pm 1$ vortex beams.

The Bloch wave theory of vortex beams is outlined in section 2. Results are presented for [100]-oriented, body centred cubic Fe and are divided into four sections. Following a brief summary of Bloch wave characteristics at 200 kV (section 3.1), section 3.2 discusses $m = 1$ vortex beam propagation between atom columns. The electron beam/specimen parameters are identical to the multislice simulations reported in reference [13]. This serves to verify the Bloch wave model, as well as provide a guide to vortex beam propagation in ‘free space’, which can then be compared to channeling along an atom column (section 3.3), the main topic of this paper. Vortex beams of different size are simulated and it is found that channeling is indeed enhanced when the probe wavefunction is similar to the 2p-type Bloch states. In section 3.4 the simulations are extended to vortex beams with larger winding number ($m = 5$), in the context of nanoparticle manipulation. Finally section 4 summarises the main conclusions from this paper.

2. Background theory and simulation method

Within the probe forming aperture the vortex wavefunction has the form $A(\mathbf{k}_t)\exp(im\Phi)$, where Φ is the azimuthal angle for the transverse wavevector component \mathbf{k}_t . $A(\mathbf{k}_t)$ is unity for all \mathbf{k}_t within the aperture and zero outside it. Fourier transforming gives the vortex wavefunction $\psi(\mathbf{R})$ in real space [21]:

$$\psi(\mathbf{R}) = \alpha i^m \exp(im\varphi) \int_0^{k_{\max}} J_m(2\pi kR) k dk \quad (1)$$

where k is the magnitude of the transverse wavevector, which has a maximum value of k_{\max} due to the aperture. J_m is a m -order Bessel function of the first kind and φ is the azimuthal angle of the two-dimensional position vector \mathbf{R} . α is a normalisation constant for the probe intensity. It is assumed throughout that the probe forming lens is aberration free, so that phase shifts due to lens distortions can be ignored. To simulate the probe using Bloch waves note that each partial plane wave of wavevector \mathbf{k}_l within the aperture will excite a given set of Bloch waves depending on the boundary conditions, i.e. the unscattered beam at the specimen entrance surface has unit amplitude and phase $m\Phi$, while all diffracted beams have zero amplitude. The excitation of the j^{th} Bloch wave is then given by $e^{im\Phi}\varepsilon_o^j(\mathbf{k}_l)$, where $\varepsilon_o^j(\mathbf{k}_l)$ is the excitation for a conventional ($m=0$) wavevector. The total wavefunction $\psi(\mathbf{R},z)$ for a probe incident at \mathbf{R}_o is given by the coherent superposition of all Bloch waves excited by the individual partial plane waves within the aperture [17]:

$$\psi(\mathbf{R}, z) = \beta \int A(\mathbf{k}_l) e^{im\Phi} \left\{ \sum_j \sum_{\mathbf{g}} \varepsilon_o^j(\mathbf{k}_l) C_g^j(\mathbf{k}_l) e^{2\pi i \mathbf{g} \cdot \mathbf{R}} e^{2\pi i \gamma^j(\mathbf{k}_l) z} \right\} e^{2\pi i \mathbf{k}_l \cdot (\mathbf{R} - \mathbf{R}_o)} d\mathbf{k}_l \quad (2)$$

here C_g^j and γ^j are the coefficients and change in longitudinal wavevector component due to channeling for the j^{th} Bloch wave. β is the normalisation constant for the probe intensity. Summations are carried out with respect to individual Bloch waves (j) and reciprocal vectors (\mathbf{g}). The z -axis is parallel to the optic axis, with the sample entrance surface at $z=0$ and points within the sample corresponding to $z>0$.

The expectation value for the L_z angular momentum operator is given by [13]:

$$\langle L_z \rangle = -i\hbar \int \psi^* \frac{\partial \psi}{\partial \varphi} d\tau \quad (3)$$

where $d\tau$ denotes an infinitesimal volume element for a 3D wavefunction or an infinitesimal area element for a 2D wavefunction (this paper only deals with the latter). For an electrostatic potential field with circular symmetry $\langle L_z \rangle$ is equal to $m\hbar$ [13]. From Eq. (3) the angular momentum contribution of the j^{th} -Bloch state can be defined (in units of \hbar) as either the integral of $(b^j)^*(\partial\psi/\partial\varphi)$ or $\psi^*(\partial b^j/\partial\varphi)$, where b^j is the net wavefunction due to the j^{th} Bloch wave in a focussed probe containing many incident wavevectors (i.e. Eq. (2) but with fixed j). In fact none of these definitions are physically meaningful, although they share the common property that when summed over all Bloch states the result equals the winding number m for the vortex beam. A more suitable definition for the angular momentum contribution due to a given Bloch state is therefore:

$$\langle L_z \rangle^j = -\frac{i\hbar}{2} \int \left[(b^j)^* \frac{\partial \psi}{\partial \varphi} + (\psi^*) \frac{\partial b^j}{\partial \varphi} \right] d\tau \quad (4)$$

The above equation can be further divided into contributions due to the Bloch wave interfering with itself (so-called ‘self’ terms, $\langle L_z \rangle_{\text{self}}^j$) and due to interference with all other Bloch states (so-called ‘cross’ terms, $\langle L_z \rangle_{\text{cross}}^j$):

$$\begin{aligned} \langle L_z \rangle_{\text{self}}^j &= -i\hbar \int (b^j)^* \frac{\partial b^j}{\partial \varphi} d\tau \\ \langle L_z \rangle_{\text{cross}}^j &= -\frac{i\hbar}{2} \int \left[(b^j)^* \frac{\partial (\psi - b^j)}{\partial \varphi} + (\psi - b^j)^* \frac{\partial b^j}{\partial \varphi} \right] d\tau \end{aligned} \quad (5)$$

The significance is that the self-terms are largely depth independent [18-19], so that any depth variation is due to the cross-terms.

Apart from Bloch state contributions it will also be useful to examine real space contributions to $\langle L_z \rangle$. Using (R, φ) polar coordinates Eq. (3) can be expressed as:

$$\langle L_z \rangle = -i\hbar \int R \left[\int \psi^* \frac{\partial \psi}{\partial \varphi} d\varphi \right] dR \quad (6)$$

Since $\langle L_z \rangle$ is a real number the second integral within the square brackets in Eq. (6) must be a pure imaginary number. This can be formally proved, since integration by parts gives:

$$\begin{aligned} \int_{-\pi}^{\pi} \psi^* \frac{\partial \psi}{\partial \varphi} d\varphi &= [\psi \cdot \psi^*]_{-\pi}^{\pi} - \int_{-\pi}^{\pi} \psi \frac{\partial \psi^*}{\partial \varphi} d\varphi \\ &= - \int_{-\pi}^{\pi} \psi \frac{\partial \psi^*}{\partial \varphi} d\varphi \end{aligned} \quad (7)$$

Note that $[\psi \cdot \psi^*]$ is the local electron intensity which is a single valued function. The left and right hand side integrands are complex conjugates of one another, so that Eq. (7) can only be true if the two integrals are pure imaginary. Therefore a new function $A(R)$ can be defined, which represents in real space the radial contribution to the vortex beam angular momentum:

$$A(R) = -i\hbar R \int \psi^*(R, \varphi) \frac{\partial \psi(R, \varphi)}{\partial \varphi} d\varphi \quad (8)$$

Results are presented for [100]-oriented Fe, with the probe either incident between the atom columns or on an atom column (points A and B in Fig. 1 respectively). The accelerating voltage and semi-convergence angles for the different $m = 1$ probes simulated in this study

are: (i) 200 kV, 10 mrad, (ii) 200 kV, 30 mrad and (iii) 600 kV, 15 mrad. 276 partial plane waves were used to simulate probe (i), while for probes (ii) and (iii) the number of partial plane waves was 648. 121 Bloch states and Doyle-Turner [22] atom scattering factors were used in the calculation. Numerical convergence was confirmed by comparing the wavefunctions from Eqs. (1) and (2) at the specimen entrance surface ($z=0$). For simplicity absorption and other forms of inelastic scattering within the specimen are neglected. In order to calculate $\langle L_z \rangle$ the wavefunction was sampled over a 6\AA radius (centred about the beam incident position) at 0.2\AA resolution for probe (i) and over a 4\AA radius at 0.07\AA resolution for probes (ii) and (iii). In addition two further $m = 5$ probes with 10 mrad (484 partial plane waves) and 20 mrad (648 partial plane waves) semi-convergence angles are also simulated at 200 kV. For calculating $\langle L_z \rangle$ the wavefunction was sampled over a 10\AA radius at 0.25\AA resolution for the first probe and a 5\AA radius at 0.1\AA resolution for the second probe. All $A(R)$ plots were calculated at 0.1\AA resolution in R .

3. Results

3.1 Bloch waves in [100]-Fe

Before presenting results for dynamic scattering, it is useful to examine the nature of [100]-Fe Bloch waves for normal incidence at 200 kV. Figure 2 plots the intensity of the important (for this paper) Bloch waves within the [100]-Fe unit cell (Fig. 1). Following convention the Bloch waves are arranged in descending order of γ^j . In this scheme Bloch waves that are tightly bound to the atom columns are at the top of the list, while more dispersive Bloch states occur further down. According to Buxton *et al* [23] an atom column orbital with n, l quantum numbers has l number of azimuthal nodal lines (fixed φ , variable R), due to the wavefunction exhibiting a $\cos(l\varphi)$, or equivalently $\sin(l\varphi)$ dependence, while the number of radial nodal lines (fixed R , variable φ) is $(n-l-1)$. On this basis Bloch wave 1 (Fig. 2a) is assigned the 1s state, while Bloch wave 5 (Fig. 2b) corresponds to 2s. The s-states are characterised by intensity maxima at the atom column positions. Bloch wave 1 is degenerate with Bloch wave 2 for all incident wavevectors, and the two only differ in the phase of the wavefunction, rather than the intensity. The 2p states are ideally given by Bloch waves 6 and 7 (Figs. 2e and 2f respectively), although Bloch waves 3 and 4 (Figs. 2c and 2d respectively) show similar characteristics, the main difference being the intensity between neighbouring atom column ‘orbitals’, due to some degree of ‘molecular bonding’. Bloch waves 3 and 4 are degenerate for all incident wavevectors, while Bloch waves 6 and 7 are only degenerate at special wavevectors, such as normal incidence (see also Figs. 3a and 3b). Note that the comparison between Bloch waves in a periodic crystal and isolated atom column orbitals is only approximate, the similarity breaking down for closely spaced atom columns of low atomic number and/or low accelerating voltages [23]. Furthermore, highly dispersive Bloch waves have no direct resemblance to atom column orbitals, since in this case the coupling of the Bloch wave to the crystal is relatively weak.

Table 1 lists the γ^j values for the first 12 Bloch states in [100]-Fe under 200 kV, normal beam incidence; as will be seen later the separation in γ^j values determines the pendellösung for the

intensity and $\langle L_z \rangle$ expectation value as the vortex beam propagates through the crystal. Dispersion surfaces along the 200 and 220 reciprocal vectors are shown in Figures 3a and 3b respectively. The non-1s states are densely grouped together, but there is a large difference in γ' between these states and the tightly bound 1s state.

3.2 $m = 1$ vortex probe incident between atom columns

The normalised intensity of the 200 kV, $m = 1$ vortex probes with 10 and 30 mrad semi-convergence angles are shown superimposed in Figure 4, plotted as a function of radial distance from the vortex centre. The intensity of the 10 mrad probe peaks at ~ 1 Å, and has a similar full width at half-maximum (FWHM). On the other hand the peak intensity position and FWHM of the 30 mrad probe is only 0.3 Å. Figure 4 also shows the integrated radial intensity distribution for Bloch wave 6 (Fig. 2e), which is taken to represent the 2p Bloch states. The radial distance here is measured with respect to an atom column and the ‘anomalous’ increase in the integrated intensity for distances larger than ~ 1 Å is due to overlap with neighbouring atom columns. The 30 mrad probe has a similar peak intensity position and FWHM compared to the 2p Bloch state, while the 10 mrad probe is significantly broader and peaks at a larger distance.

The $\langle L_z \rangle$ and intensity pendellösung for the 10 mrad probe is shown in Figures 5a and 5b respectively. The probe is incident between the atom columns, i.e. point A in Fig. 1. The intensity is calculated within a 2 Å radius, an area that encloses the first peak of the vortex probe at the specimen entrance surface (Fig. 4). Note that $\langle L_z \rangle$ at the specimen entrance surface (0.94) is slightly less than unity; the result can be improved if the probe wavefunction is sampled at higher spatial resolution, although this significantly increases the computation time, without altering the fundamental physics. The $\langle L_z \rangle$ pendellösung is similar to the multislice result in reference [13], which suggests that the Bloch wave simulations are indeed valid. Note that both the $\langle L_z \rangle$ and intensity pendellösung have maxima and minima at approximately the same depths within the specimen, as first noted in [13].

Figure 6 shows plots for $A(R)$ and $\langle L_z \rangle$ Bloch state contributions at the specimen entrance surface, the first pendellösung minimum ($z=60$ Å) and first maximum ($z=100$ Å). The Bloch state contributions are divided into self and (self+cross)-terms, the former being largely depth independent. $A(R)$ at the specimen entrance surface has a similar form to the probe intensity profile (Fig. 4) as required, and $\langle L_z \rangle$ is due mainly to the first 12 Bloch states. The fact that cross terms make up a significant fraction of the angular momentum suggests large variations in $\langle L_z \rangle$ with respect to depth, as is indeed the case in Fig. 5a. At $z=60$ Å, the $A(R)$ plot (Fig. 6c) shows a distinct negative peak at ~ 1.4 Å, which is also evident for $z=100$ Å (Fig. 6e), although the sign of the peak is reversed. In fact for all $\langle L_z \rangle$ pendellösung minima this peak was negative, and vice-versa for $\langle L_z \rangle$ maxima. A similar trend was observed with respect to the 1s Bloch state contribution to $\langle L_z \rangle$ (Figs. 6d and 6f). The $A(R)$ peak at ~ 1.4 Å is largely due to the 1s Bloch state, since this is the distance between the probe centre and the nearest neighbour atom columns (Fig. 1). Confirmation of this was obtained by removing the 1s Bloch state from the simulations and noting the suppression of the 1.4 Å peak, as well as by

comparing the area under the 1.4 Å peak to the 1s state $\langle L_z \rangle$ contribution (the two values were similar). The 1s $\langle L_z \rangle$ contribution is however due to interference with other non-1s states, the self-interference term being negligible. From Table 1 interference of the 1s Bloch state with (say) any of Bloch waves 3 to 7 gives a depth periodicity of $\sim 85\text{-}91$ Å, which is similar to that observed in Figs. 5a and 5b (note that this calculation does not take into account any dispersion in γ^j). Intensity oscillations are due to the 1s and non-1s states going in and out of phase with depth, and the results suggest that a similar effect may be responsible for the $\langle L_z \rangle$ pendellösung. The small wavelength of the oscillation is due to the relatively large separation between 1s and other Bloch states (Fig. 3).

It is important to clarify the nature of the angular momentum transfer that gives rise to the $\langle L_z \rangle$ pendellösung. Although the depth variation in $\langle L_z \rangle$ is due to Bloch wave interference, no momentum is actually transferred between the Bloch states, but rather momentum is exchanged between the crystal and overlapping Bloch wavefunctions [13]. In other words the self-interference $\langle L_z \rangle$ terms are depth independent for a given Bloch wave, so that its angular momentum is constant. This is somewhat similar to Bragg diffraction in a perfect crystal, where intensity transfer between the unscattered and diffracted beams is due to Bloch wave interference, although the excitation of the Bloch states remain unchanged. However, Bloch state excitations can vary in a deformed crystal (for the case of small strains this is given by the well known Howie-Whelan equations [14]), as well as doped crystals [15], due to intra- and inter-band scattering. The change in excitation will lead to momentum transfer between Bloch states, although the net change in momentum must be zero.

3.3 $m = 1$ vortex probe incident on an atom column

Figure 7a shows the $\langle L_z \rangle$ pendellösung for the $m=1$, 10 mrad vortex probe incident on an atom column (point B in Fig. 1), calculated for depths of up to 1000 Å. Since $\langle L_z \rangle$ was calculated over a circular area of only 6 Å radius, there will be some inaccuracy at larger depths, due to probe broadening. In fact at 1000 Å depth the integrated intensity of the probe within a 6 Å radius was 82% of that at the specimen entrance surface. Furthermore, inelastic thermal diffuse scattering will also be significant at these depths, but are not taken into account. The pendellösung is consistent with the multislice simulations of Löffler and Schattschneider [13], although in that study results were only presented up to a depth of 200 Å. $\langle L_z \rangle$ consists of short wavelength oscillations superimposed on a more slowly varying, long wavelength oscillation ‘background’. The power spectrum of the pendellösung revealed two major peaks corresponding to periodicities of 91 Å and 500 Å respectively (see vertical arrows in Figure 7b). The smaller wavelength is similar to that observed for a vortex probe positioned between atom columns (for convenience, this shall be hereafter referred to as a ‘free space’ vortex probe); in fact a direct comparison of Fig. 5a and Fig. 7a shows that the minima and maxima are at approximately the same depths, but the magnitude of the $\langle L_z \rangle$ oscillations are significantly smaller for the probe incident on an atom column.

Figure 8 shows plots for $A(R)$ and Bloch state $\langle L_z \rangle$ contributions at the specimen entrance surface, and two further representative depths of $z = 230$ Å (smallest $\langle L_z \rangle$ for the first broad

minimum) and 470 Å (largest $\langle L_z \rangle$ for the subsequent broad maximum). Bloch waves 3 and 4 (2p character) are the main contributors to $\langle L_z \rangle$ at the specimen entrance surface, with Bloch wave 1 (1s) and Bloch waves 5-12 also partly contributing (Fig 8b). Compare this behaviour to the ‘free space’ vortex probe, where several Bloch states are strongly contributing (Fig. 6b). The self-interference terms for Bloch waves 3-4 and 6-7 are however small, suggesting that coupling of the $m = 1$ vortex probe to these 2p-type Bloch states is weak, which is expected given the large width of the probe (Fig. 4). Similar to the ‘free space’ probe, the short wavelength pendellösung minima and maxima correspond to negative and positive contributions of the 1s Bloch state to $\langle L_z \rangle$ (e.g. Figs. 8d and 8f). However, the magnitude of the 1s contribution is smaller, so that the pendellösung oscillations are less pronounced. Since the intensity at the vortex centre is zero, excitation of the 1s Bloch state will be weak for the atom column on which the probe is incident. A consideration of the [100]-Fe unit cell geometry (Fig. 1) indicates that the first nearest neighbour atom columns are at a distance of 2.0 Å ($=a_0/\sqrt{2}$), while the second nearest neighbours are at a distance of 2.9 Å ($=a_0$). The intensity of the 10 mrad vortex probe is however also weak at these distances (Fig. 4), so that overall the 1s Bloch state excitation, and hence its $\langle L_z \rangle$ contribution, is diminished, at least at the specimen entrance surface. In fact at the specimen entrance surface the 1s state $\langle L_z \rangle$ contribution is $0.19\hbar$ for the ‘free space’ probe, compared to only $0.05\hbar$ for the probe incident on the atom column. Although at certain depths this value can increase due to interference with other non-1s Bloch states, overall the weak excitation of the 1s Bloch state is the cause for the damping of short wavelength oscillations in the $\langle L_z \rangle$ pendellösung compared to the ‘free space’ probe.

The $A(R)$ plots at $z = 230$ Å and 470 Å (Figs. 8c and 8e respectively) show a positive peak at ~ 0.5 Å, which is largely assigned to 2p-type Bloch waves 3-4 and 6-7, that are excited at the atom column on which the probe is incident. This was confirmed by removing the 2p-type Bloch waves from the simulations and noting the suppression of the peak. At $z = 230$ Å there is a broad negative ‘plateau’ in the $A(R)$ curve, extending between ~ 2 -3 Å, i.e. between the first and second nearest neighbour atom column positions. At this depth the overall $\langle L_z \rangle$ of the beam is negative (Fig. 7a) and it is clear that the contribution from the neighbouring atom columns outweighs that of the probe incident atom column (i.e. the positive peak at ~ 0.5 Å). This is somewhat similar to the well known ‘cross-talk’ phenomenon in the intensity pendellösung for conventional ($m = 0$) focussed electron probes. Fig. 8d shows that at $z = 230$ Å the negative $\langle L_z \rangle$ is largely due to Bloch waves 8-10, as well as Bloch waves 1 and 4. At still larger depths (i.e. $z = 470$ Å) the $A(R)$ plot shows that atom columns beyond the second nearest neighbour can also contribute to the angular momentum due to further probe spreading. Furthermore, contributions from the first and second nearest neighbour atom columns do not have the same form at $z = 470$ Å, i.e. the broad negative ‘plateau’ in Fig. 8c is no longer visible.

The $\langle L_z \rangle$ pendellösung for the 10 mrad probe can now be explained as follows. Consider first the atom column on which the probe is incident. Due to the broadness of the $m = 1$ vortex beam, coupling to the 2p-type Bloch states is non-ideal and therefore other non-1s states must be excited in order to match the probe wavefunction at the specimen entrance surface.

Excitation of the 1s state is weakened (or non-existent) by the zero intensity at the vortex core. Interference of the 2p-type Bloch waves with other non-1s states gives rise to the ~ 0.5 Å peak in the $A(R)$ plots. The ‘tails’ of the vortex probe wavefunction overlap with the neighbouring atom columns, so that a mixture of 1s and non-1s Bloch states will be excited depending on the boundary conditions. During probe propagation interference of the 1s state with other non-1s states, largely along the neighbouring atom columns, gives rise to the short wavelength oscillations in $\langle L_z \rangle$. The short periodicity is due to the relatively large separation between 1s and non-1s Bloch state energies (Figs. 3a and 3b). Interference of the non-1s states on the other hand, which have similar energies, gives rise to the long wavelength oscillations in Fig. 7a. The periodicity is expected to vary between atom columns, due to different combinations of Bloch states being excited by the incident probe, although at certain depths (e.g. 230 Å) the cumulative contribution from neighbouring atom columns can be larger than that of the probe incident column. As an example, the average γ' value for Bloch waves 5-12 is -0.0041 Å⁻¹ (Table 1) and, neglecting dispersion, this gives a periodicity of 454 Å due to interference with Bloch waves 3 and 4, which is similar to the result (500 Å) obtained from Fig. 7b.

For more efficient channeling it is therefore essential that the vortex probe wavefunction is similar to the 2p-type Bloch waves. This can be achieved by using a larger aperture and increasing the probe semi-convergence angle to 30 mrad (Fig. 4). The $\langle L_z \rangle$ pendellösung for the 30 mrad, $m = 1$ probe is shown in Figure 9a. The depth is limited to 200 Å due to the large computation time. $\langle L_z \rangle$ values for the 10 mrad, $m = 1$ probe are also superimposed and confirm that channeling is indeed enhanced for the 30 mrad probe. Channeling can be further improved by increasing the accelerating voltage of the microscope, whilst decreasing the aperture size so that the ideal probe wavefunction is maintained. The larger accelerating voltage means that the Bloch states are more tightly bound to the atom columns [23]. A 600 kV, 15 mrad probe was found to have a similar wavefunction to the 200 kV, 30 mrad probe and its $\langle L_z \rangle$ pendellösung is also shown in Fig. 9a. The channeling is indeed better than any of the other probes simulated.

Bloch state $\langle L_z \rangle$ contributions for the 200 kV, 30 mrad and 600 kV, 15 mrad probes at the specimen entrance surface are shown in Figs. 9b and 9c respectively. An important criterion for channeling is that the cumulative sum of the self-interference terms for individual Bloch states must constitute a large fraction of the overall angular momentum. This ensures that $\langle L_z \rangle$ for the vortex beam is largely depth independent. Indeed for the 600 kV, 15 mrad probe the total self-interference contribution is $0.36\hbar$, compared to only $0.27\hbar$ for the 200 kV, 30 mrad probe (for the 200 kV, 10 mrad probe however the corresponding value is $-0.20\hbar$). Out of this $0.26\hbar$ is due to 2p-type Bloch waves for the 600 kV, 15 mrad probe, compared to an equivalent value of only $0.19\hbar$ for the 200 kV, 30 mrad probe. The 200 kV, 30 mrad probe has large $\langle L_z \rangle$ contributions (Fig. 9b) from not only 2p-type Bloch waves 3-4 and 6-7, but also Bloch wave 5 (2s character; note that the angular momentum generated by Bloch wave 5 is due to interference with other Bloch states). At 600 kV Bloch waves 3 to 6 are all 2p-type and Fig. 9c shows that these are the main contributors to the vortex angular momentum. Due to the higher accelerating voltage the more tightly bound 2p-type Bloch waves at 600 kV

have a similar profile to the equivalent atomic column orbitals, unlike, for example, Bloch waves 3 and 4 at 200 kV (Figs. 2c and 2d). This may explain the enhanced coupling to the probe wavefunction at 600 kV.

With conventional ($m=0$) focussed electron probes a smaller aperture size leads to a larger depth of field with respect to the intensity profile. The depth of field is proportional to λ/θ^2 , where λ is the electron wavelength and θ is the probe semi-convergence angle. It is interesting to speculate if a similar phenomenon occurs in the $\langle L_z \rangle$ pendellösung for the 600 kV, 15 mrad and 200 kV, 30 mrad probes, i.e. if the *overall* shape of the pendellösung for the former probe varies more slowly with respect to depth (the beam energy is thought to have a second-order effect compared to the aperture size, based on the depth of field for a conventional probe). Some evidence for this effect is observed by comparing Figs. 9b and 9c. Many more Bloch states contribute to the 200 kV, 30 mrad probe angular momentum compared to the 600 kV, 15 mrad probe, meaning that the long wavelength oscillations in $\langle L_z \rangle$ due to interference of 2p-type Bloch waves with other non-1s states should be less pronounced for the latter. Overall this results in a ‘flatter’ $\langle L_z \rangle$ pendellösung for the 600 kV, 15 mrad probe, with some short wavelength oscillations due to interference of the weakly excited 1s states with non-1s states (Figs. 9a and 9c; the 1s states at 600 kV correspond to Bloch waves 1 and 2). However, to conclusively demonstrate the depth of field effect the $\langle L_z \rangle$ pendellösung must be calculated to much larger depths than in Fig. 9a. This is computationally demanding with Bloch waves, especially for atomic scale vortex probes, but considerably faster using multislice. Furthermore, multislice can also correctly model the thermal diffuse scattering at larger specimen depths using the frozen phonon method, thereby improving the accuracy of $\langle L_z \rangle$ (with Bloch waves thermal diffuse scattering leads to a depletion of the electron intensity).

Finally in EMCD measurements EELS spectra from both $m = \pm 1$ vortex probes must be acquired. However, simulations show that the $\langle L_z \rangle$ pendellösung for the $m = -1$ probe is simply the negative of the $\langle L_z \rangle$ pendellösung for $m = 1$. This is easily understood since the chirality of the phase spiral is reversed for the two vortices, so that the azimuthal derivative $\partial/\partial\phi$ in $\langle L_z \rangle$ (Eq. 3) changes sign as well, although the absolute value is unchanged. Dynamic scattering of the $m = -1$ probe is therefore equivalent to $m = 1$.

3.4 momentum transfer for a $m = 5$ vortex probe

Unlike EMCD the objective of nanoparticle manipulation is to transfer momentum from the incident electrons to the specimen as efficiently as possible, i.e. over the dimensions of the nanoparticle. The angular momentum due to the electromagnetic field of the vortex electrons is considerably smaller than that due to its mass flux [7], so that only the $\langle L_z \rangle$ pendellösung need be considered. From previous results it is clear that efficient momentum transfer is achieved through interference of the 1s state with other non-1s states, thereby giving rise to short wavelength oscillations in the $\langle L_z \rangle$ pendellösung. To confirm this $m=5$ vortex beams with two different convergence semi-angles (i.e. 10 and 20 mrad) are simulated at 200 kV. The radial intensity distributions at the specimen entrance surface for the two probes, as

determined by Eqs. (1) and (2), are shown superimposed in Figures 10a and 10b respectively. In both cases the Bloch wave solution diverges slightly from the ‘optical’ solution (i.e. Eq. (1)), especially when reproducing the subsidiary maxima. Increasing the number of Bloch waves and number of partial plane waves within the aperture did not improve the convergence significantly. Furthermore, the convergence deteriorates further for vortex probes of still higher winding number (e.g. $m = 10$). It is suggested that this could be due to inaccuracies in the (parameterised) Doyle-Turner atom scattering factors [22] used in the Bloch wave calculation, especially with regards to the atom scattering factors at small scattering angles, which are related to the long range electrostatic potential.

Figure 11a shows the $\langle L_z \rangle$ pendellösung for the two probes and Figs. 11b and 11c show the individual Bloch state $\langle L_z \rangle$ contributions at the specimen entrance surface for the 10 and 20 mrad probes respectively. The probes are incident along an atom column in [100]-Fe (point B in Fig. 1), although the incident position within the unit cell should not be critical, since the probe spans several neighbouring atom columns. Short wavelength oscillations with large amplitude are observed in the 10 mrad probe pendellösung, but these are damped for the 20 mrad probe. The wavelength is similar to what has been observed previously for 1s and non-1s Bloch state interference (Figs. 5a and 7a). A comparison of Figs. 11b and 11c show that for the 20 mrad probe the 1s state $\langle L_z \rangle$ contribution is smaller than the 10 mrad probe, so that the oscillations are diminished as required. Figs. 11b and 11c show several other interesting trends as the aperture size is increased. First the $\langle L_z \rangle$ contribution of 1s and other tightly bound Bloch states (e.g. Bloch waves 3 and 4) decrease at the expense of *many* high index, dispersive Bloch states, that are only weakly coupled to the atom columns. The Bloch state $\langle L_z \rangle$ contributions for a 200 kV, $m = 5$, 30 mrad probe at the specimen entrance surface are shown in Fig. 11d and confirms that this trend holds true for larger apertures as well. Secondly the cumulative sum of Bloch wave self-interference $\langle L_z \rangle$ terms increases monotonically with aperture size, e.g. for the $m = 5$ probes discussed here the total self-interference contribution is $0.31\hbar$, $0.68\hbar$ and $0.79\hbar$ for the 10, 20 and 30 mrad probes respectively. This suggests that probe coupling is strongest to many high index Bloch states, rather than a Bloch wave of particular character, such as 2p-type for $m = 1$ vortex probes.

The above trends can be rationalised by considering the mathematical form of the vortex probe wavefunction as given by Eq. (1). For large values of m , the Bessel function $J_m(2\pi kR)$ peaks at large values of kR . As the aperture size is increased the main peak of the vortex beam shifts to lower values of R (Figs. 10a and 10b) and in this case it is the wavevectors with large transverse component that contribute most strongly to this peak. Tightly bound Bloch states, such as 1s, are strongly excited close to normal incidence, while dispersive Bloch states are excited during tilted illumination [19]. For large apertures the main peak of the vortex beam, and consequently a large fraction of its angular momentum, is therefore due to the dispersive Bloch states, with the 1s state becoming progressively less important. The numerical results also show that large angular momentum vortex beams couple more efficiently to the dispersive states, rather than 1s or 2p-type non-dispersive states, which have smaller intrinsic angular momentum. Furthermore, the coupling is with many Bloch states, in

contrast to small angular momentum vortex beams which couple to only a few states of well defined character.

Efficient momentum transfer therefore requires small probe forming apertures to generate large amplitude, short wavelength depth oscillations in $\langle L_z \rangle$ due to interference of 1s and non-1s Bloch states. However, the crucial parameter is the $\langle L_z \rangle$ value at the specimen exit surface, which should ideally be zero so that all of the beam angular momentum is transferred to the sample upon transmission. This is not always possible to achieve with a rapidly oscillating $\langle L_z \rangle$ pendellösung. It should also be mentioned that the above calculations assume a semi-infinite sample with flat, parallel free surfaces. More work is required to determine how dynamic scattering is affected by the shape and size of the nanoparticle that is being manipulated. Furthermore, it could be argued that the simulations assumed static atoms, although the nanoparticle will rotate during angular momentum transfer from the beam. A momentum transfer of $5\hbar$ from a single incident electron will result in a rotation period of 4×10^{-4} s for a 10 nm diameter Fe-nanoparticle. This is many orders of magnitude longer than the time it takes for the electron to traverse through the particle (5×10^{-17} s for a 200 kV beam), so that the atom configuration is effectively 'frozen' for the incident electron. The momentum transfer increases linearly with the beam current and exposure time, but frictional damping from the support substrate [6] means that the rotation period is considerably longer than even the calculated value for a single electron. The static atom approximation is therefore justified for typical experimental conditions.

4. Conclusions

Vortex beam scattering in a crystal has been analysed using Bloch waves for the two scenarios of EMCD and nanoparticle manipulation, the latter using high angular momentum vortex beams. For a $m = \pm 1$ beam incident on an atom column (as in EMCD) the $\langle L_z \rangle$ pendellösung consists of short and long wavelength oscillations. The short wavelength oscillations are due to interference of the 1s Bloch state with non-1s states, and can be minimised by selecting a suitable probe forming aperture, so that the probe wavefunction approximately matches that of the 2p-type Bloch states. Coupling can also be enhanced by increasing the accelerating voltage so that the 2p-type Bloch states are more tightly bound to the atom columns. On the other hand small probe forming apertures are desirable for high angular momentum vortex beams and nanoparticle manipulation, since then the 1s state is strongly excited and interference with non-1s states gives rise to short wavelength oscillations in the $\langle L_z \rangle$ pendellösung. This enables efficient angular momentum transfer between the incident electrons and the sample.

Acknowledgements

BGM would like to thank Durham University for granting research leave.

References

- [1] M. Uchida, and A. Tonomura, *Nature (London)* **464**, 737 (2010).
- [2] J. Verbeeck, H. Tian, and P. Schattschneider, *Nature (London)* **467**, 301 (2010).
- [3] B.J. McMorran, A. Agrawal, I.M. Anderson, A.A. Herzing, H.J. Lezec, J.J. McClelland, and J. Unguris, *Science* **331**, 192 (2011).
- [4] J. Verbeeck, P. Schattschneider, S. Lazar, M. Stöger-Pollach, S. Löffler, A. Steiger-Thirsfeld, and G. Van Tendeloo, *Appl. Phys. Lett.* **99**, 203109 (2011).
- [5] J. Verbeeck, H. Tian, and A. Béché, *Ultramicroscopy* **113**, 83 (2012).
- [6] J. Verbeeck, H. Tian, and G. Van Tendeloo, *Adv. Mater.* **25**, 1114 (2013).
- [7] S.M. Lloyd, M. Babiker, and J. Yuan, *Phys. Rev. A* **88**, 031802 (2013).
- [8] A. Béché, R. Van Boxem, G. Van Tendeloo, and J. Verbeeck, *Nature Physics* **10**, 26 (2014).
- [9] S. Lloyd, M. Babiker, and J. Yuan, *Phys. Rev. Lett.* **108**, 074802 (2012).
- [10] J. Yuan, S.M. Lloyd, and M. Babiker, *Phys. Rev. A* **88**, 031801 (2013).
- [11] J. Ruzs, and S. Bhowmick, *Phys. Rev. Lett.* **111**, 105504 (2013).
- [12] P. Schattschneider, S. Löffler, M. Stöger-Pollach, and J. Verbeeck, *Ultramicroscopy* **136**, 81 (2014).
- [13] S. Löffler, and P. Schattschneider, *Acta Cryst. A* **68**, 443 (2012).
- [14] P.B. Hirsch, A. Howie, R.B. Nicholson, D.W. Pashley, and M.J. Whelan, *Electron Microscopy of Thin Crystals* (Butterworths, Great Britain, 1965).
- [15] B.G. Mendis, *Acta Cryst. A* **64**, 613 (2008).
- [16] B.G. Mendis, *Acta Cryst. A* **66**, 407 (2010).
- [17] S.J. Pennycook, and D.E. Jesson, *Ultramicroscopy* **37**, 14 (1991).
- [18] P.D. Nellist, and S.J. Pennycook, *Ultramicroscopy* **78**, 111 (1999).
- [19] Y. Peng, P.D. Nellist, and S.J. Pennycook, *J. Electron Microsc.* **53**, 257 (2004).
- [20] H. Xin, and H. Zheng, *Microsc. Microanal.* **18**, 711 (2012).
- [21] P. Schattschneider, and J. Verbeeck, *Ultramicroscopy* **111**, 1461 (2011).
- [22] P.A. Doyle, and P.S. Turner, *Acta Cryst. A* **24**, 390 (1968).
- [23] B.F. Buxton, J.E. Loveluck, and J.W. Steeds, *Phil. Mag. A* **38**, 259 (1978).

Figure captions

Figure 1: Unit cell of body centred cubic-Fe in [100] orientation. Projected atom columns are depicted by the filled circles. Simulations are carried out for vortex beams incident between the atom columns (point ‘A’ marked by a cross) and on the atom column marked ‘B’.

Figure 2: Bloch wave intensity profiles for a 200 kV, $m=0$ beam at normal incidence in [100]-Fe. The intensity is plotted over the [100]-Fe unit cell (Fig. 1). (a) to (f) correspond to Bloch waves 1 (1s character), 5 (2s), 3 (2p), 4 (2p), 6 (2p) and 7 (2p). The Bloch waves are arranged in descending order of γ^j .

Figure 3: Bloch wave dispersion surfaces for [100]-Fe at 200 kV along (a) 200 and (b) 220 reciprocal lattice vectors. In each case the longitudinal wavevector (in inverse Angstroms) for the Bloch wave is plotted against the transverse component of the incident wavevector (normalised with respect to the reciprocal lattice vector). Bloch waves 1 and 2 are degenerate

and form the upper curve in the dispersion surface. For ease of visualisation lower lying Bloch states that are degenerate at normal beam incidence are depicted by dashed lines; this includes Bloch waves 3-4 (degenerate at all incident wavevectors) and Bloch waves 6-7.

Figure 4: Radial intensity profiles for 200 kV, $m = 1$ vortex probes with 10 and 30 mrad semi-convergence angles. Also superimposed is the integrated radial intensity distribution for the p-type Bloch wave 6 (the origin is at an atom column); note that at large (>1 Å) radial distances the integrated intensity of the Bloch wave is complicated by overlap with neighbouring atom columns. In each case the peak intensity has been normalised for ease of visualisation.

Figure 5: (a) $\langle L_z \rangle$ and (b) intensity pendellösung for a 200 kV, 10 mrad semi-convergence angle, $m = 1$ vortex probe incident between the atom columns in [100]-Fe (i.e. point A in Fig. 1). $\langle L_z \rangle$ is plotted in units of \hbar and the intensity is integrated over a 2 Å radius about the vortex centre.

Figure 6: $A(R)$ and Bloch state $\langle L_z \rangle$ contributions for a 200 kV, 10 mrad, $m = 1$ vortex probe incident between the atom columns. The $A(R)$ plots at depths of $z = 0, 60$ and 100 Å are shown in (a), (c) and (e) respectively, while the corresponding Bloch state $\langle L_z \rangle$ contributions (in units of \hbar) at the same depths are shown in (b), (d) and (f) respectively. Bloch state contributions are divided into self and (self+cross)-interference terms. Data points are labelled as '1s' for Bloch state 1 and using vertical arrows for the 2p-type, Bloch states 3, 4, 6 and 7. Lines connecting the data points are purely for visualisation purposes.

Figure 7: (a) $\langle L_z \rangle$ pendellösung (in units of \hbar) for a 200 kV, 10 mrad semi-convergence angle, $m = 1$ vortex probe incident on an atom column in [100]-Fe (i.e. point B in Fig. 1). (b) Power spectrum of the $\langle L_z \rangle$ pendellösung in (a). The two main spatial frequencies corresponding to short and long wavelength oscillations are indicated by the vertical arrows.

Figure 8: $A(R)$ and Bloch state $\langle L_z \rangle$ contributions for a 200 kV, 10 mrad, $m = 1$ vortex probe incident along an atom column. The $A(R)$ plots at depths of $z = 0, 230$ and 470 Å are shown in (a), (c) and (e) respectively, while the corresponding Bloch state $\langle L_z \rangle$ contributions (in units of \hbar) at the same depths are shown in (b), (d) and (f) respectively. Bloch state contributions are divided into self and (self+cross)-interference terms. Data points are labelled as '1s' for Bloch state 1 and using vertical arrows for the 2p-type, Bloch states 3, 4, 6 and 7. Lines connecting the data points in the $\langle L_z \rangle$ plots are purely for visualisation purposes.

Figure 9: (a) $\langle L_z \rangle$ pendellösung (in units of \hbar) for a 200 kV, 30 mrad and 600 kV, 15 mrad vortex probe incident on an atom column in [100]-Fe. Also superimposed is the $\langle L_z \rangle$ pendellösung for the 200 kV, 10 mrad vortex probe from Fig. 7a. In each case the winding number of the vortex probe is +1. Bloch state $\langle L_z \rangle$ contributions (in units of \hbar) at the specimen entrance surface for the 200 kV, 30 mrad and 600 kV, 15 mrad probes are shown in (b) and (c). Data points are labelled as '1s' for Bloch state 1 and using vertical arrows for the

2p-type, Bloch states. Lines connecting the data points in (b) and (c) are purely for visualisation purposes.

Figure 10: Radial intensity distributions for 200 kV, $m = 5$ vortex probes with (a) 10 mrad and (b) 20 mrad semi-convergence angle. The solid line is the solution obtained from Eq. (1), while the dashed line represents the Bloch wave solution (Eq. 2). The peak intensities have been normalised for visualisation.

Figure 11: (a) $\langle L_z \rangle$ pendellösung for 200 kV, $m = 5$ vortex probes with 10 mrad and 20 mrad semi-convergence angle. The probes are incident on an atom column position in [100]-Fe. Bloch state $\langle L_z \rangle$ contributions for the 10 and 20 mrad probes at the specimen entrance surface are shown in (b) and (c) respectively. (d) shows the Bloch state $\langle L_z \rangle$ contributions for a 200 kV, $m = 5$ vortex probe with 30 mrad semi-convergence angle. $\langle L_z \rangle$ was calculated by sampling the wavefunction over a 5 Å radius at 0.1 Å resolution. In all figures $\langle L_z \rangle$ is expressed in units of \hbar . Lines connecting the data points in (b), (c) and (d) are purely for visualisation purposes.

Tables

Bloch state	γ -value (\AA^{-1})
1 and 2 (1s; degenerate)	0.0091
3 and 4 (2p; degenerate)	-0.0019
5 (2s)	-0.0020
6 and 7 (2p; degenerate)	-0.0026
8	-0.0033
9	-0.0043
10 (3s)	-0.0047
11-12 (degenerate)	-0.0062

Table 1: [100]-Fe Bloch state γ -values for normal incidence at 200 kV. Bloch wave character and degeneracy at normal beam incidence are as indicated.

Figures

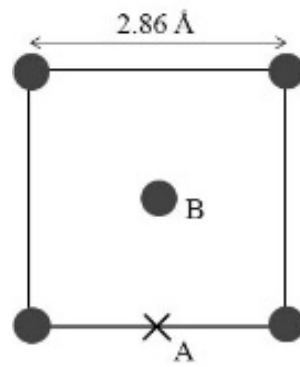


Figure 1

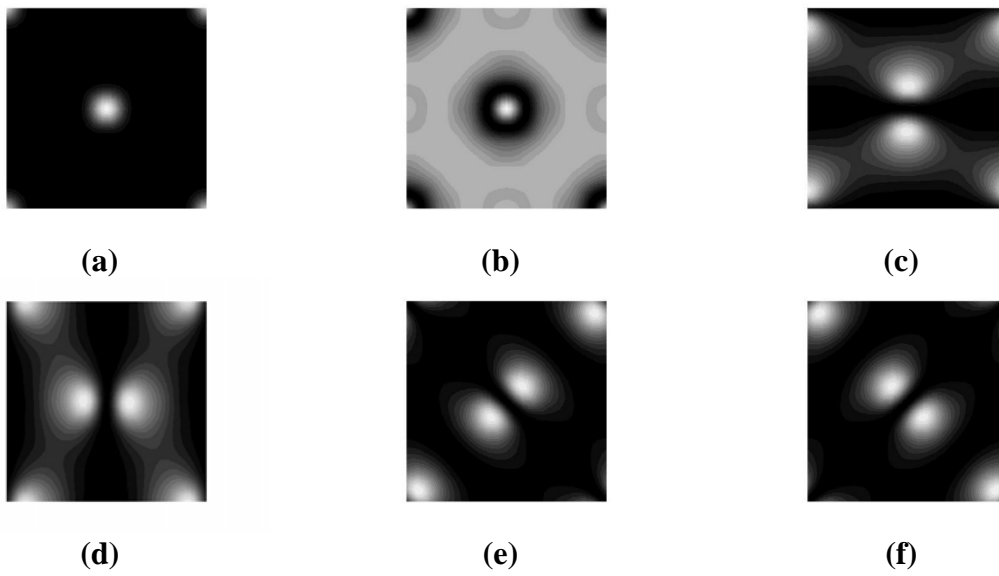


Figure 2

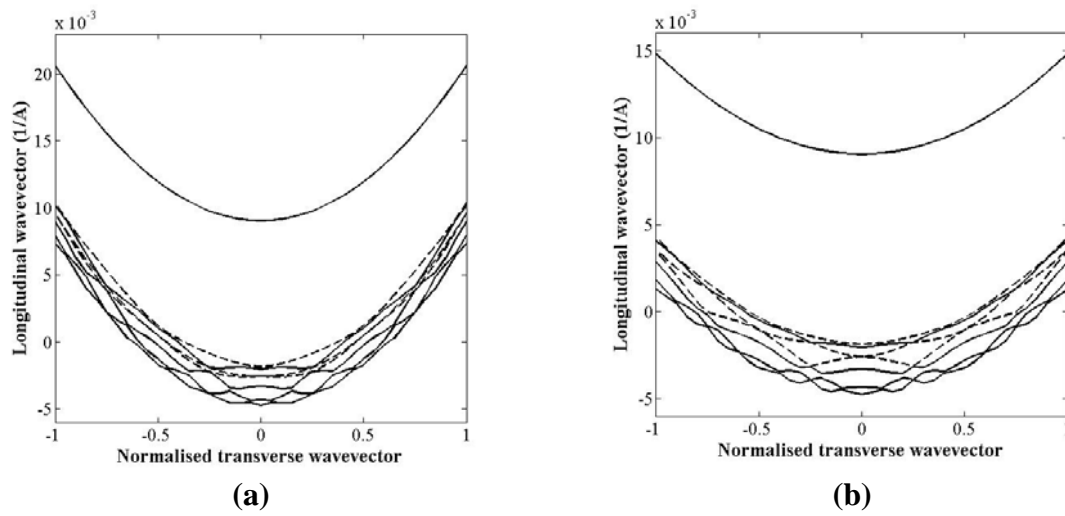


Figure 3

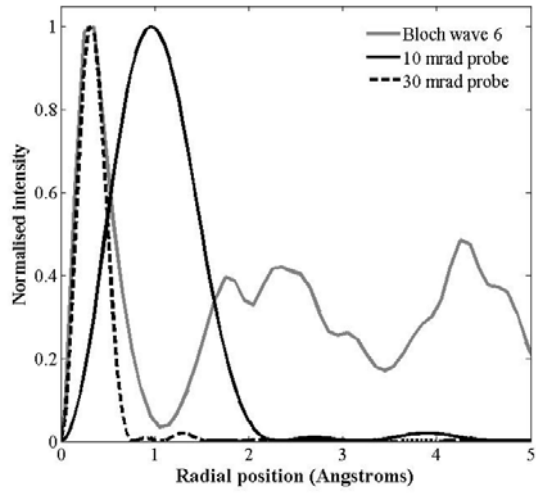
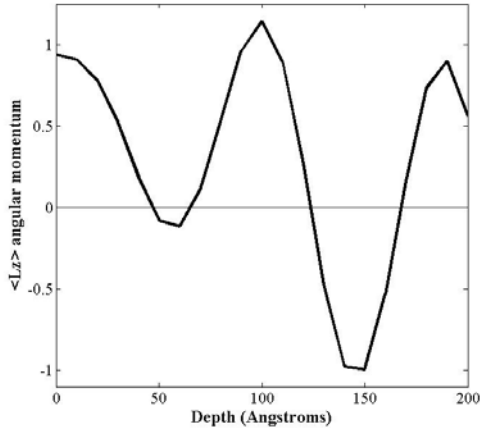
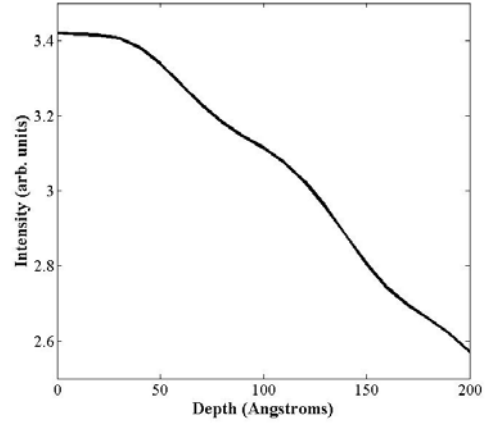


Figure 4

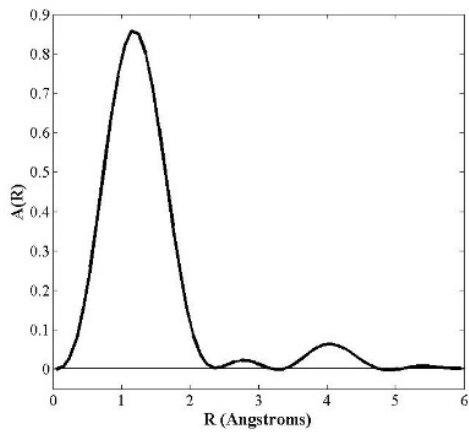


(a)

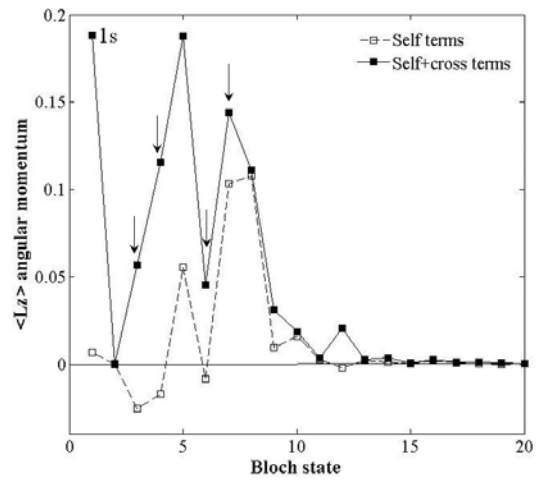


(b)

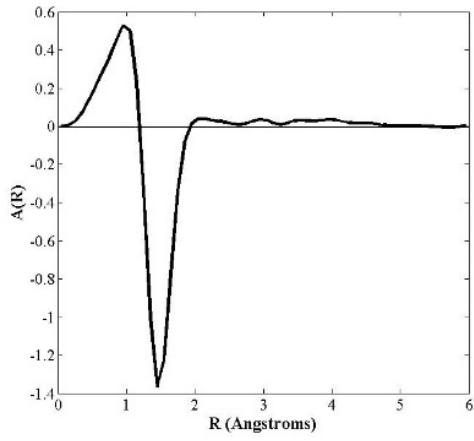
Figure 5



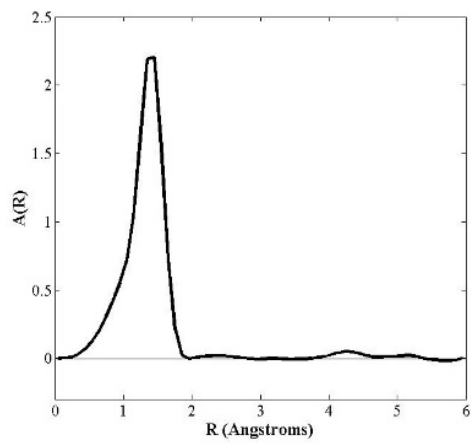
(a)



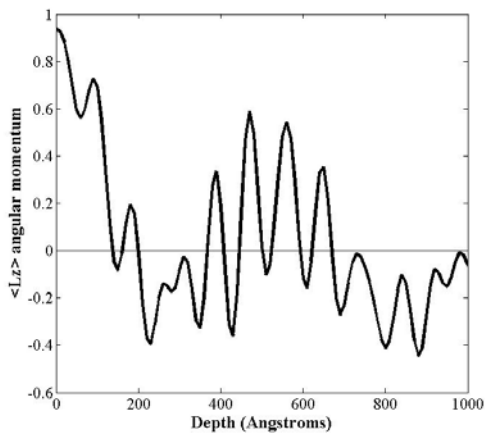
(b)



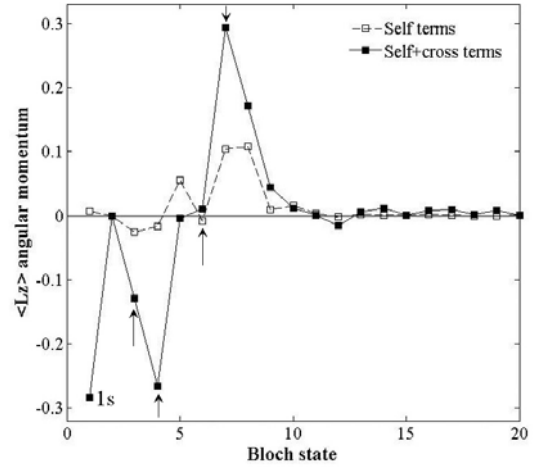
(c)



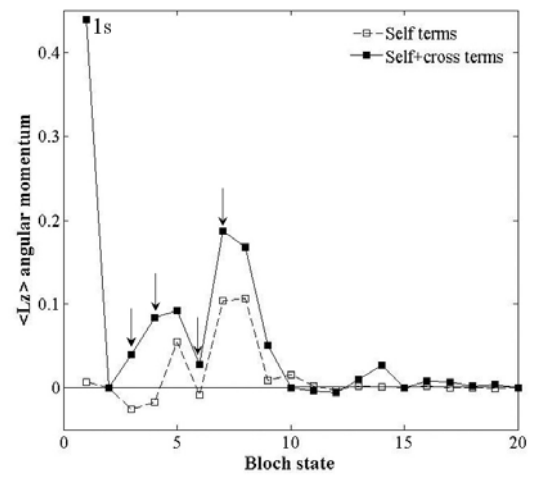
(e)



(a)

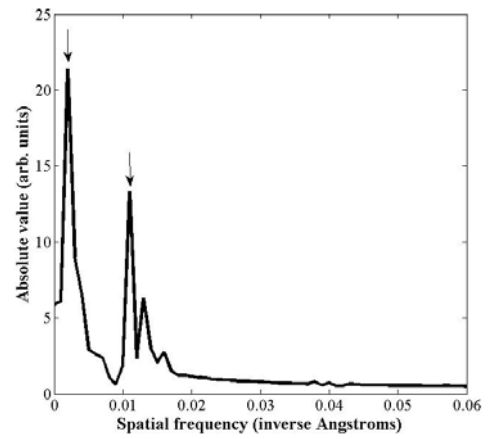


(d)



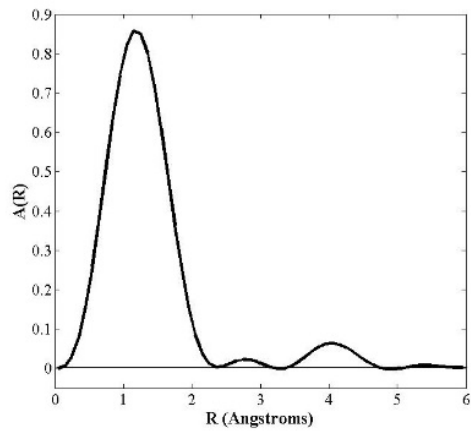
(f)

Figure 6

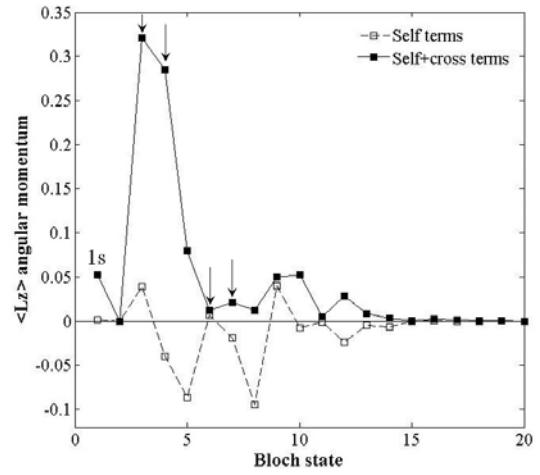


(b)

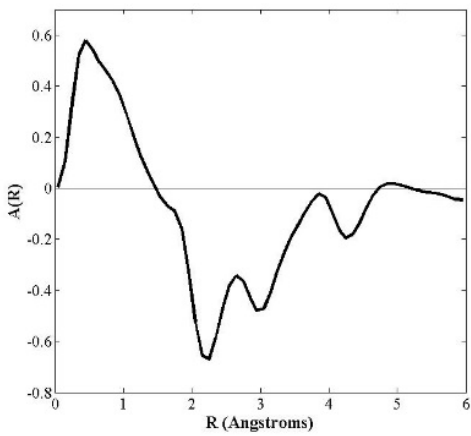
Figure 7



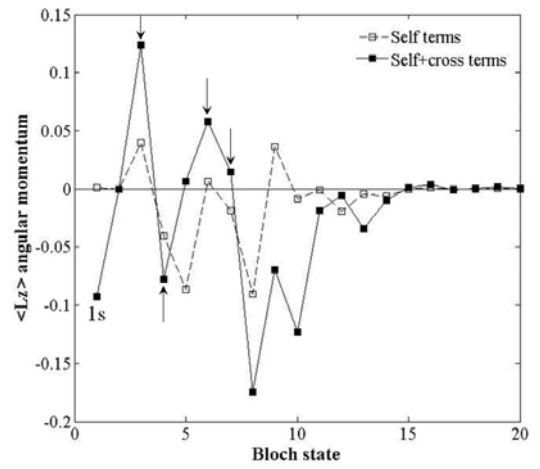
(a)



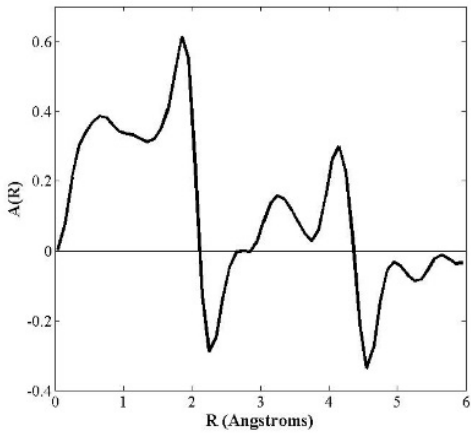
(b)



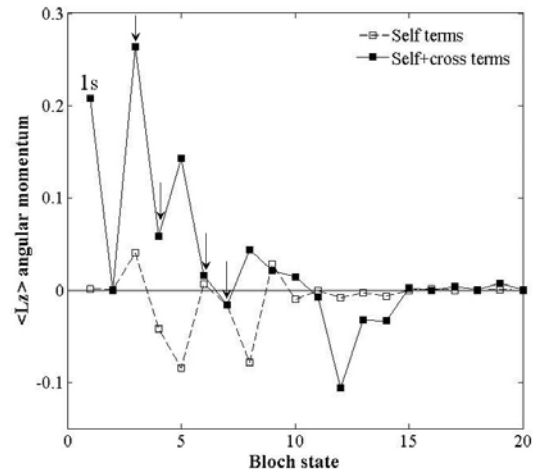
(c)



(d)

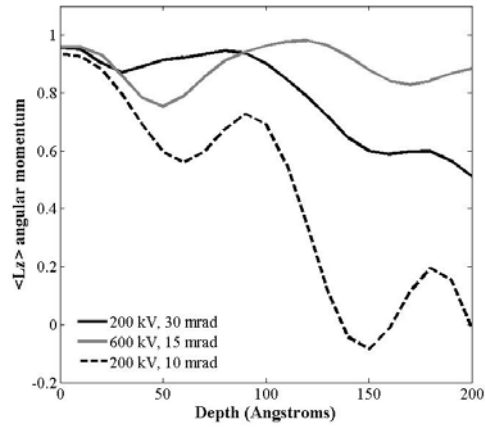


(e)

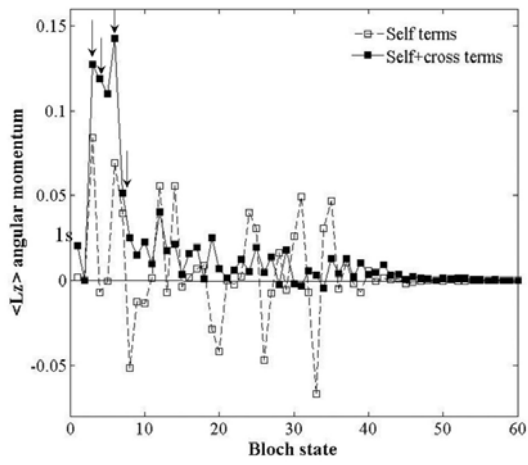


(f)

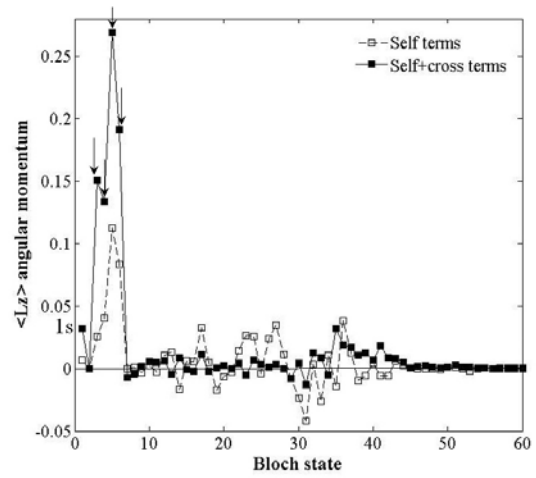
Figure 8



(a)

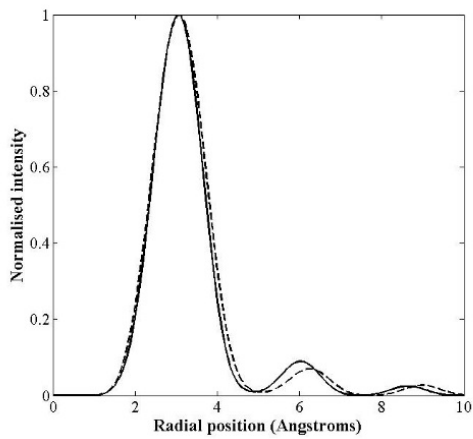


(b)

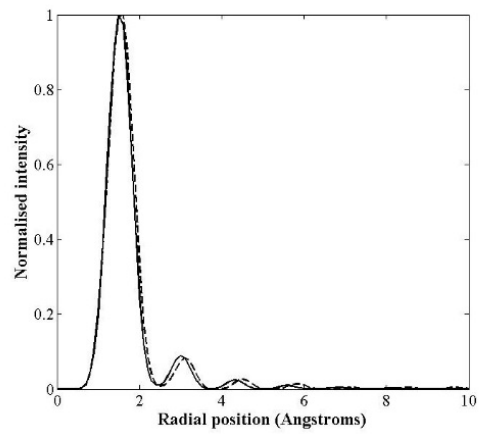


(c)

Figure 9

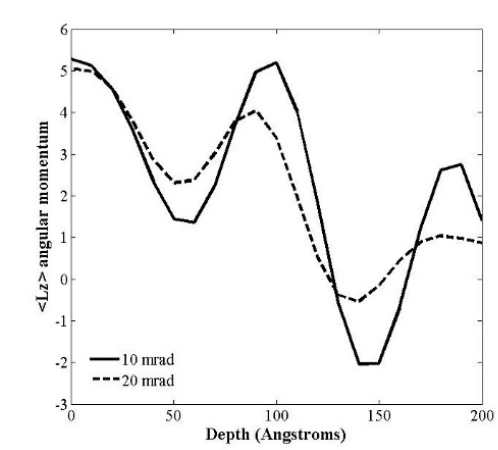


(a)

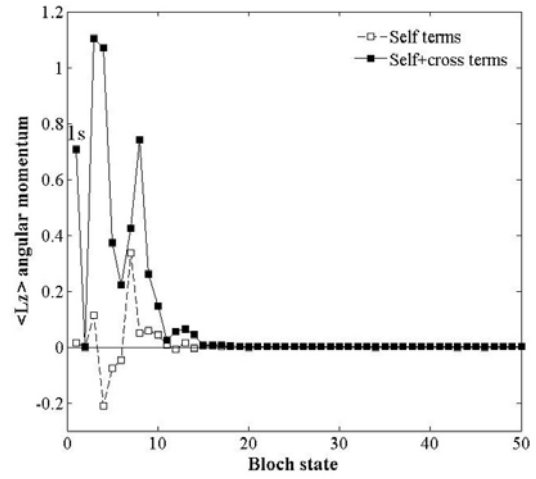


(b)

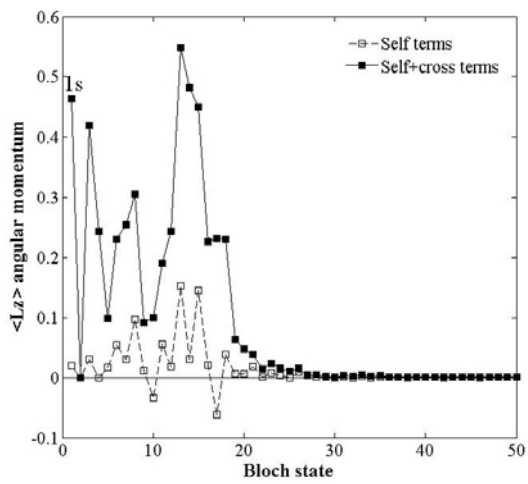
Figure 10



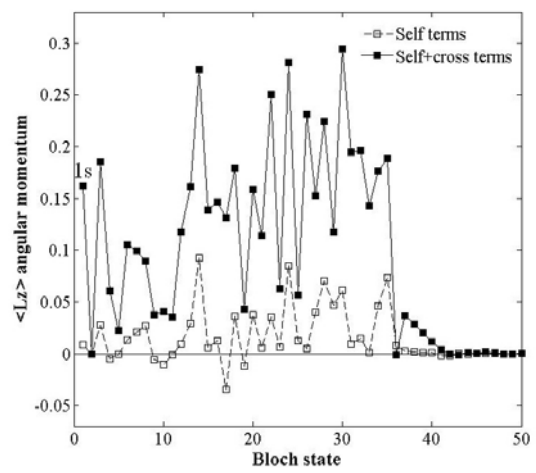
(a)



(b)



(c)



(d)

Figure 11